

Gate-tunable graphene Josephson diode effect due to magnetochiral anisotropy

Chuan-Shuai Huang

Department of Physics, Xiamen University, Xiamen 361005, China

(Dated: December 6, 2023)

Usually the magnetochiral anisotropy related Josephson diode effect is assumed to be based on conventional two-dimensional electron gas, such as the InAs quantum well. Here we propose a graphene-based Josephson junction as a broadly gate-tunable platform for achieving nonreciprocal supercurrent within the context of magnetochiral anisotropy. We show that the resulting nonreciprocal supercurrents will exhibit a sign reversal when the graphene switches from n -type doping to p -type doping. Particularly, the magnitude of the nonreciprocity is highly sensitive to the electrostatic doping level of graphene, enabling gate control of the diode efficiency from zero up to approximately 40%. This giant gate-tunability stems from the chiral nature of the pseudo-relativistic carriers in graphene, allowing the graphene Josephson diode emerges as a promising element for advanced superconducting circuits and computation devices. Moreover, we have also obtained the so-called $0 - \pi$ -like phase transitions in the current-phase relation, in coincidence with recent experimental finding.

Introduction.— Nonreciprocal transport refers to a phenomenon by which the different resistance R for electric currents traversing in different (opposite) directions, i.e., $R(+I) \neq R(-I)$. When both time-reversal and inversion symmetry are simultaneously broken in spatially symmetric devices, a closely related phenomenon leading to nonlinear nonreciprocal response is known as the magnetochiral anisotropy (MCA) [1–3]. This can be obtained, for example, by applying an out-of-plane electric field $\mathbf{E}||\hat{\mathbf{e}}_z$ and an in-plane magnetic field \mathbf{B} . As $\mathbf{E}||\hat{\mathbf{e}}_z$ and \mathbf{B} are orthogonal to each other and to the direction along which current is traversing, the current-dependent resistance can be described as $R = R_0[1 + \gamma\hat{\mathbf{e}}_z(\mathbf{B} \times \mathbf{I})]$, where γ is the MCA rectification coefficient depending on the Rashba spin-orbit coupling (RSOC) strength [4].

The MCA related nonreciprocity has also been observed in noncentrosymmetric superconductors under magnetic fields, where the resulting nonreciprocal supercurrent is known as the superconducting diode effect (SDE) characteristic by finite momentum Cooper pairing [5]. The SDE allows for a larger critical supercurrent in one direction than in the opposite, offering numerous novel device applications in superconducting spintronics and quantum computing technology [6]. Similarly, the MCA could also induce SDE in superconducting-normal-superconducting (SNS) Josephson junctions, a phenomenon referred to as the Josephson diode effect (JDE) [7–10].

From the microscopic point of view, JDE is more conveniently described by Andreev bound states (ABSs) [11–14]. These bound states, in the presence of Zeeman coupling and resonant spin-orbital coupling (RSOC), modify the current-phase relation (CPR), imparting an anomalous phase shift ϕ_0 ($\phi_0 \neq 0, \pi$) [15–17]. Such a phase shift leads to a marked asymmetry of the CPR, that is, $I(\phi) \neq I(-\phi)$. In addition to the ϕ_0 -phase shift, another

essential component required to exhibit the diode effect is a skewed CPR, namely, a CPR with higher harmonics, as those observed in short-ballistic junctions with high transparency[18]. To be more specific, the Fourier expansion of the CPR can be written as

$$I(\phi) = \sum_n [a_n \sin(n\phi) + b_n \cos(n\phi)], \quad (1)$$

where a_n and b_n decrease with n . The combination of RSOC and in-plane Zeeman field will enhance the even terms [i.e., $b_n \cos(n\phi)$ component] owing to the broken

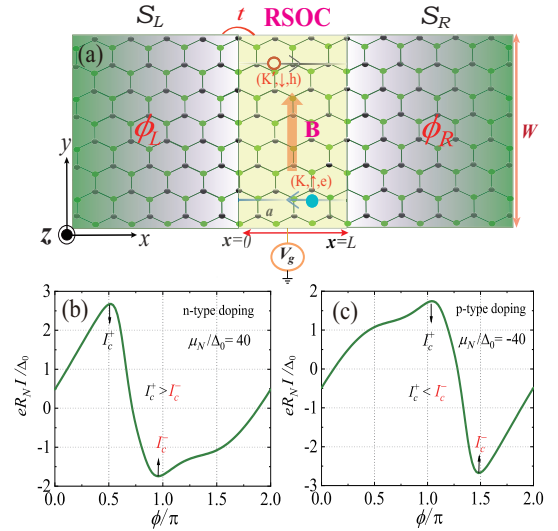


FIG. 1: (a) Schematic diagrams of a short SNS junction formed on a single layer graphene, where proximity-induced in-plane Zeeman field and RSOC are applied in the central N region ($0 < x < L$). The electrically tunable gate V_g is used to adjust the doping level in graphene. (b)-(c) Calculated CPR for graphene with n -type doping and p -type doping. The parameters are $\mu_N = \pm 40\Delta_0$, $m_y = t_R = 10\Delta_0$, $L = 100$, and $T/T_c = 0.1$. R_N represents the Sharvin resistance of a perfectly transparent graphene junction in the normal state.

* Electronic mail: 19820220157176@stu.xmu.edu.cn

inversion and time-reversal symmetries [19]. In order to obtain the JDE, it is concurrently essential that the a_n coefficients should be non-zero for $n > 1$, and not too small compared to a_1 . That is, the CPR must be skewed already in zero in-plane field.

Experimentally, the JDE was first realized by Baumgartner et al. in a symmetric Al/InAs/Al junction [20]. Hitherto, all the reported MCA related Josephson diodes have been fabricated based on conventional two-dimensional electron gas (2DEG) [19–22], where the gate-tunability of the diode efficiency is not immediately evident. In this letter, we propose a graphene SNS junction as a new platform for achieving JDE in the context of MCA effect, which is feasible in an actual tunneling experiment, since the enhanced RSOC and Zeeman coupling in graphene have been achieved by means of the proximity effect [23–30]. As illustrated in Fig. 1(a), a tunable gate voltage V_g can be applied in the non-superconducting graphene region (N region) to modulate the electrostatic doping. In Figs. 1(b) and 1(c), one can observe that the nonreciprocal critical currents (I_c^+ and I_c^-) between the n -type and p -type doped cases are opposite, suggesting a promising way to manipulate the JDE by switching the charge carrier type through electrostatic gating. As we will also demonstrate in the following text, such a graphene-based Josephson diode contains giant gate-tunability due to the pseudo-relativistic chiral property of Dirac fermions in graphene, setting it apart from conventional 2DEG systems. We also emphasize that the underling physical mechanism behind the JDE proposed here is not the finite Cooper pair momentum, but rather the phase interference between the first-order and second-order harmonics.

Model and formalism.— Our starting point is the nearest-neighbor tight-binding Hamiltonian of the central N region that incorporates both effects of RSOC t_R and in-plane Zeeman field m_y [31, 32]

$$H = -t \sum_{\langle i,j \rangle \alpha} c_{i\alpha}^\dagger c_{j\alpha} - \mu_i \sum_{i\alpha} c_{i\alpha}^\dagger c_{i\alpha} - m_y \sum_{i\alpha\beta} c_{i\alpha}^\dagger \sigma_y c_{i\beta} + it_R \sum_{\langle i,j \rangle \alpha\beta} c_{i\alpha}^\dagger (\vec{\sigma} \times \vec{d}_{ij})_{\alpha\beta}^z c_{j\beta}, \quad (2)$$

where $c_{i\alpha}^\dagger$ ($c_{i\alpha}$) is the electron creation annihilation operator with spin α on site i , $\vec{\sigma} = (\sigma_x, \sigma_y, \sigma_z)$ is the Pauli matrix describing the electron's spin, and the angular bracket $\langle i, j \rangle$ stands for a pair of nearest-neighboring sites. The first term represents the nearest-neighbor hopping with hopping energy t . The second term describes the chemical potential. We will assume that the chemical potential in the superconducting regions, denoted as μ_S , is rather large and constant due to the external contacts, while in the N region, the doping level μ_N can be varied arbitrarily with a local back-gate denoted by V_g [33–35]. The third term is the Zeeman coupling induced by an in-plane magnetic-field $\mathbf{B} = B\vec{e}_y$ directed in the y direction.

Although the g factor in graphene is much smaller than in Rashba nanowires, the magnetic-field-induced Zeeman field has been achieved in graphene with considerable magnitudes through a strong exchange coupling with a magnetic insulator, such as EuS under an applied magnetic field [28–30]. The fourth term represents the extrinsic RSOC associated with the nearest-neighbor hopping. The vector \vec{d}_{ij} represents the unit vector connecting two sites i and j . Experimentally, the coupling strength t_R can arise up to the order of 10 meV by growing graphene on Ni(111) intercalated with a Au layer or proximity to high SOC transition-metal dichalcogenides [24–27].

In the two superconducting regions, an on-site s -wave pair potential of $V_{pair}^{L(R)} = \sum_i \Delta e^{i\phi_{L(R)}} (c_{i\uparrow}^\dagger c_{i\downarrow}^\dagger + \text{H.c.})$ is introduced by proximity to external superconducting contacts [36, 37], but the RSOC and Zeeman coupling are absent. Here, $L(R)$ denotes the left (right) lead. The temperature dependence of the BCS gap reads $\Delta(T) = \Delta_0 \tanh(1.74\sqrt{T/T_c - 1})$ with $\Delta_0 = 1.76k_B T_c$ being the zero-temperature superconducting gap and T_c being the critical temperature. In addition, $\phi_{L(R)}$ denotes the phase of pair potential in the $L(R)$ superconducting lead. In our numerical calculation, the hopping energy is set to be $t = 1$ eV for the sake of simplicity, the pair potential at zero temperature is fixed at $\Delta_0 = 0.001t$ and taken as the energy unit of parameters. In the numerical treatment, we assume clean, smooth interfaces, allowing a Fourier transform along the direction parallel to the interface is applicable. In addition, the type of interface can vary, but having an in-situ pairing ensures that the direction of the interface is immaterial. We will here use the armchair-type interface and one unit cell is $\sqrt{3}a/2$ long.

The supercurrent through l -th column in the central N region can be evaluated by the recursion Green's function as follows [38, 39]:

$$I = \frac{1}{h} \int_{-\infty}^{+\infty} dE \sum_{k_y} \text{Tr}[H_{l,l+1} \tilde{e} G_{l+1,l}^<(E, k_y) - \tilde{e} H_{l+1,l} G_{l,l+1}^<(E, k_y)], \quad (3)$$

where $k_y = 2\pi n/W$ is the transverse momentum with n being an integer since the junction width is assumed to be large enough ($W \gg L$) [40], $\tilde{e} = -e\tau_3 \otimes \sigma_0$ denotes the charge matrix, τ_3 is the third Pauli matrix in Nambu space, and σ_0 is the unit matrix in the spin space. $H_{l,l+1}$ is the Hamiltonian matrix element, representing the coupling between the l -th and $l+1$ -th layer in the N region. The lesser-than Green's function in the equilibrium state satisfies $G^< = (G^r - G^a)f(E)$ with $f(E)$ being the Fermi-Dirac distribution function. The retarded and advanced Green's functions read $G^r = (G^a)^\dagger = [\hat{E}I - H_N - \Sigma_L^r - \Sigma_R^r]^{-1}$, where H_N is the Hamiltonian of the N region. The retarded self-energy Σ_L^r (Σ_R^r) due to the coupling with the S_L (S_R) region could be obtained by the recursive method [41, 42]. Similar to the supercurrent, the ABS spectra can also be numerically calculated

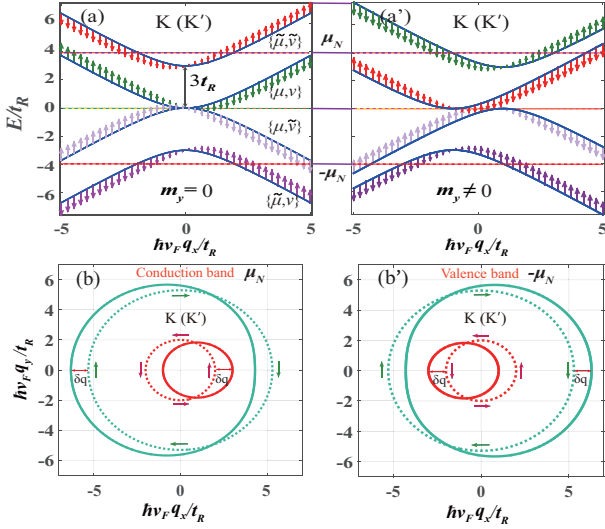


FIG. 2: Band structure of graphene with a RSOC in the low energies near the Dirac points for (a) $m_y = 0$ and (a') $m_y = t_R$. The arrows denote the calculated \mathbf{q} -dependent in-plane polarization of electron spins in the eigenstates of the Hamiltonian. (b)-(b') The schematic illustration of non-trivial in-plane spin-textured Fermi contour of the Rashba-Zeeman graphene in the (q_x, q_y) -space. Polarizations are identical in K and K' valleys. External circles: $\mu = +1$; internal circles: $\mu = -1$.

using the Green's function method. Since the ABSs correspond to particle density peaks within the superconducting gap, the energy levels of ABSs can be located by searching the peaks of the particle density at column l in the central N region

$$\rho_l = -\frac{1}{\pi} \text{Im}\{\text{Tr}[G^r(l, l)]\} \quad (4)$$

at a given macroscopic superconducting phase difference $\phi = \phi_R - \phi_L$.

Band structures and ABS spectra.— Here we are only interested in the transport channels near the Dirac points with low-energy electron dispersion. In the weak limit of magnetic field $m_y/t_R \rightarrow 0$, this spectrum can be formulated as

$$E_{\mu\nu} = \mu\nu\sqrt{(\hbar v_F q)^2 + \lambda_R^2} - \mu\lambda_R, \quad (5)$$

where $q = \sqrt{q_x^2 + q_y^2}$ is the momentum measured from the K and K' points so that $|q|a \ll 1$, $\lambda_R = 3t_R/2$ represents the effective strength of the RSOC, μ, ν is the band indices and v_F is the Fermi velocity, given by $v_F = 3at/2$ with a value $v_F \simeq 1 \times 10^6 \text{ m/s}$. The corresponding electronic spectrum consists of four energy bands, which are plotted in Fig. 2(a). In our notation, we define $\mu = \nu = +1$ and $\tilde{\mu} = \tilde{\nu} = -1$, such that $\mu\nu = 1$ or $\tilde{\mu}\tilde{\nu} = 1$ refers to the conduction bands while $\mu\tilde{\nu} = -1$ or $\tilde{\mu}\nu = -1$ refers to the valence bands. The in-plane spin

polarizations are determined by the expectation values of $\vec{\sigma}$ in the state $\psi_{\mu\nu}$ for $m_y = 0$ is given by [43]

$$\mathbf{S}_{\mu\nu}(\mathbf{q}) \equiv \langle \psi_{\mu\nu} | \vec{\sigma} | \psi_{\mu\nu} \rangle = \frac{\mu \hbar v_F (\mathbf{q} \times \hat{\mathbf{z}})}{\sqrt{\lambda_R^2 + (\hbar v_F q)^2}}. \quad (6)$$

\mathbf{S} depends on the wave vector and is proportional to the group velocity $\mathbf{v}_{\mu\nu}(\mathbf{q}) = \partial E_{\mu\nu} / \hbar \partial \mathbf{q}$. The sign of μ in Eq. (7) signifies the helical direction of the spin textures, which is identical for valleys K and K'. In a y -direction in-plane Zeeman field, each subband is shifted in energy, $E'_{\mu\nu}(\mathbf{q}) - E_{\mu\nu}(\mathbf{q}) = \langle \psi_{\mu\nu} | m_y \sigma_y | \psi_{\mu\nu} \rangle$, rendering the MAC effect of the energy spectrum. The magnitude of the momentum shift is estimated by its Fermi-surface average,

$$\delta q_{\mu\nu} \simeq \frac{\langle \psi_{\mu\nu} | m_y \sigma_y | \psi_{\mu\nu} \rangle_{\text{FS}}}{\langle \psi_{\mu\nu} | v_{\mu\nu} | \psi_{\mu\nu} \rangle_{\text{FS}}}. \quad (7)$$

with $\hat{\mathbf{x}}$ being the unit direction vector point to the x -axis. Such a momentum shift will result in a remarkable Cooper pair momentum during the Andreev reflection process within each FS, leading to a phase shift for the related ABS, as shown in Fig. 3.

In the short junction limit ($L \ll \xi$), the two FS-resolved ABSs at $k_y = 0$ are in a rough approximation-simulated as [12–14]

$$\varepsilon_{\mu\nu} = \pm \Delta \sqrt{1 - \tau_{\mu\nu} \sin^2(\phi/2 + \delta\phi_{\mu\nu}/2)}, \quad (8)$$

where $\tau_{\mu\nu}$ is the transmission probability for normal-state electrons to tunnel through the junction in channels with a state $\psi_{\mu\nu}$, $\delta\phi_{\mu\nu} = 2\delta q_{\mu\nu}L$ denotes the extra shift phase resulting from the momentum change of $\delta q_{\mu\nu}$. Due to the opposite momentum shifts between the two spin-splitting FSs, the two FS-resolved ABSs experience opposite phase shifts. The phase derivative of the ABS spectra eventually defines the CPR [44, 45]:

$$I(\phi) \simeq -\frac{2e}{\hbar} \sum_{\mu\nu} \frac{\partial \varepsilon_{\mu\nu}}{\partial \phi} \tanh(\varepsilon_{\mu\nu}/2k_B T). \quad (9)$$

Let us first consider the case of n -type doping, where the Fermi level locates at the conduction bands with two subbands $\{\mu, \nu\}$ and $\{\tilde{\mu}, \tilde{\nu}\}$. Then the total current can be expressed as $I(\phi) = I_{\mu\nu} + I_{\tilde{\mu}\tilde{\nu}}$. Both $I_{\mu\nu}$ and $I_{\tilde{\mu}\tilde{\nu}}$ can be decomposed into a series of different orders of harmonics with an anomalous shift of each term:

$$\begin{aligned} I_{\mu\nu} &\simeq a_1 \sin(\phi + \delta\phi_{\mu\nu}) + a_2 \sin(2\phi + 2\delta\phi_{\mu\nu}) + \dots, \\ I_{\tilde{\mu}\tilde{\nu}} &\simeq \tilde{a}_1 \sin(\phi + \delta\phi_{\tilde{\mu}\tilde{\nu}}) + \tilde{a}_2 \sin(2\phi + 2\delta\phi_{\tilde{\mu}\tilde{\nu}}) + \dots, \end{aligned} \quad (10)$$

where the higher-order sine terms with $n > 2$ have been neglected. We notice that the signs of phase shifts are opposite between $I_{\mu\nu}$ and $I_{\tilde{\mu}\tilde{\nu}}$, i.e., $\delta\phi_{\mu\nu} = -\delta\phi_{\tilde{\mu}\tilde{\nu}}$. This phase shift is essentially equivalent to the cosine term in Eq. (1). The second order sine term $a_2(\tilde{a}_2)$ is sensitive to graphene's electrostatic doping level μ_N and determines the skewedness of CPR, deviating significantly from a simple sinusoidal form. It should be emphasized that the

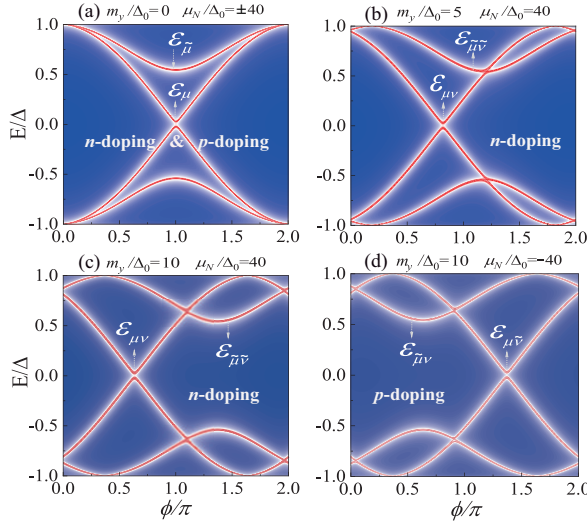


FIG. 3: Numerically calculated energy levels of ABSs as functions of the superconducting phase difference ϕ at $k_y = 0$. The related parameters are denoted in the figure; other parameters are the same as those in Figs. 1(b) and 1(c).

RSOC gap, i.e., $E_{\mu\nu} - E_{\bar{\mu}\bar{\nu}} = 3t_R$, is specific to graphene and could act as a spin-dependent potential that affects the spin-splitting ABS $\varepsilon_{\mu\nu}$, resulting in the amplitude difference between $I_{\mu\nu}$ and $I_{\bar{\mu}\bar{\nu}}$. Consequently, the total CPR has the form of $I(\phi) = I_1 \sin(\phi + \delta\phi_1) + I_2 \sin(2\phi + \delta\phi_2)$. Here, the relative phase difference between the I_1 and I_2 , given by $\delta = 2\phi_1 - \delta\phi_2$, plays a crucial role in the JDE. This difference is explicitly determined by both the m_y -induced momentum shift and the RSOC-induced spin-splitting gap.

On the contrary, the Fermi level in p -doped graphene is now located in valence bands indicated by $\bar{\mu}\bar{\nu}$ and $\bar{\mu}\nu$. As illustrated in Fig. 2(b'), the Zeeman shifts for the valence bands always contrasts to that in the conduction bands, resulting in opposite phase shifts. In this scenario, we can describe the total CPR as $I(\phi) = I_1 \sin(\phi - \delta\phi_1) + I_2 \sin(2\phi - \delta\phi_2)$ where the sign of $\delta\phi_{1(2)}$ has been changed when compared to the n -doped case. It follows that the nonreciprocity-related factor δ will also change sign and then reverses the diode effect, leading to $I_c^+ < |I_c^-|$ instead of $I_c^+ > |I_c^-|$. Such a sign reversal can be also interpreted by the phase-dependent free energy $F(\phi)$ that can be found in the Supplemental Material.

Evolution of CPR and Quality factor. — Now we proceed to analysis the evolution of CPRs by varying μ_N , as shown in Fig. 4(a). We have made the simplifying assumption that the doping profile changes abruptly from μ_S to μ_N at the interface. To ensure the validity of our results, we limit our analysis to $t_R \leq 10$ meV, which has been experimentally verified to be feasible. It is evident that $I(\phi)$ at $\mu_N = 5\Delta_0$ appears as a nearly sinusoidal function with an additional slight phase shift, namely, $I(\phi) = I_1 \sin(\phi + \phi_0)$ with $I_2 \rightarrow 0$. Ac-

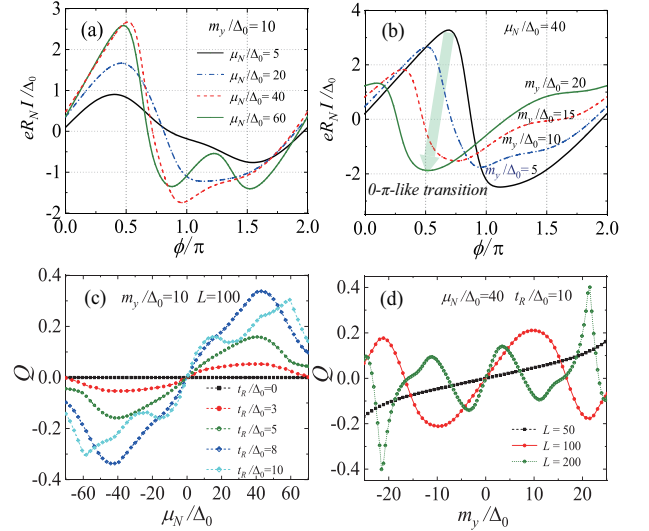


FIG. 4: Calculated CPRs for (a) several μ_N at $m_y = 10\Delta_0$ and (b) several m_y at $\mu_N = 40\Delta_0$; other parameters are the same as those in Figs. 1(b) and 1(c). Quality factor of JDE Q as a function of (c) doping level μ_N for serval t_R and (d) Zeeman coupling strength m_y for serval L .

tually, the diode effect is usually not apparent in the weak doping limit ($\mu_N/\Delta_0 \sim 1 - 5$) wherein both the two spin-splitting channels are in the low $\tau_{\mu\nu}$ limit due to the nearly zero carrier density. In this regime, the higher harmonics and the associated skewedness of CPR are strongly suppressed, thereby alleviating the diode effect. Interestingly, increasing μ_N can significantly enhance $\sin(2\phi)$ terms in Eq. (13), resulting in a remarkable enhancement of the diode effect. Such an enhancement becomes even clearer when plotting the diode quality factor $Q = (I_c^- - |I_c^-|)/(I_c^+ + |I_c^-|)$ as a function of μ_N shown in Fig. 4(c). The symmetry relation $Q(\mu_N)$ and $Q(-\mu_N)$ is satisfied and Q is highly sensitive to the electrostatic doping level μ_N as well as t_R . It might be worth mentioning here that Q remains zero at $\mu_N = 0$ regardless of the change in t_R , which is a direct consequence of the vanishing of all $\mathbf{S}_{\mu\nu}(\mathbf{q} \rightarrow 0)$ at the Dirac points. The diode quality increases linearly with increasing $|\mu_N|$, and Q can be as large as 35% at a moderate doping level. This suggests that our proposed setup contains a large gate-tunability, making it an ideal material for designing electrically tunable JDEs with numerous benefits for practical superconducting diode devices.

However, Q will be drastically reduced when μ_N is larger than some critical values (e.g., $\mu_N > 6t_R$). It is reasonable to speculate that in the large limit of μ_N , i.e., $\mu_N \gg t_R$, the RSOC would play only a very minor role for the total Josephson current. To further illustrate the evolution of the quality factor with the variation of parameters, in Fig. 4(d), we show the dependence of Q as a function of m_y for serval junction lengths count by the number of the unit cell L (1 unit cell = 1.23\AA). Similar to the case of varying μ_N , one can see that the

nonreciprocity efficiency is also an odd function of m_y , namely, $Q(m_y) = -Q(-m_y)$. The magnitude of Q depends strongly on the Zeeman coupling strength. In the context of a very short junction length, e.g., $L = 50$, the diode effect shows a linear increase with m_y within a relatively large range. However, this is not the case for moderate junction length, e.g., $L = 100$, in that periodic sign reversals of Q can be found with the increase in $|m_y|$. This can be intuitively understood from the $0 - \pi$ -like phase transition at relatively large Zeeman field as illustrated in Fig. 4(b). More precisely, the phase shift of $I_{\mu\nu}$ is proportional to the production of m_y and L , i.e., $\delta\phi_{\mu\nu} \propto m_y L / \hbar v_F$. When m_y is large enough that $\delta\phi_{\mu\nu}$ equals approximately $(2n + 1)\pi$, the SNS junction might undergo current-reversing $0 - \pi$ -like phase transitions, leading to sign changes of $Q(m_y)$. These phase transition associated sign reversals are in coincidence with the

recently conducted Josephson diode experiment based on 2DEG under large in-plane fields. However, we emphasize that the undamped-periodic oscillation of $Q(m_y)$ observed in Fig. 4(d) can be significantly distinguished from the 2DEG system [21]. More details on the evolution of the system's ground states can be found in the Supplementary Information.

Conclusions — We have studied the nonreciprocal transport in a graphene Josephson junction under the magnetochiral mechanism. Our results reveal that the graphene Josephson diode exhibits giant gate-tunability, including the sign reversal by switching the graphene's doping type. Such an advantage may pave the way for applications of graphene in the field of the superconducting diode.

-
- [1] Y. Tokura and N. Nagaosa, Nat. Commun. **9**, 3740 (2018).
- [2] P. He, S. S. L. Zhang, D. Zhu, Y. Liu, Y. Wang, J. Yu, G. Vignale, and H. Yang, Nat. Phys. **14**, 495 (2018).
- [3] Y. Wang, H. F. Legg, T. Bömerich, J. Park, S. Biesenka, A. A. Taskin, M. Braden, A. Rosch, and Y. Ando, Phys. Rev. Lett. **128**, 176602 (2022).
- [4] T. Ideue, K. Hamamoto, S. Koshikawa, M. Ezawa, S. Shimizu, Y. Kaneko, Y. Tokura, N. Nagaosa, and Y. Iwasa, Nat. Phys. **13**, 578 (2017).
- [5] F. Ando, Y. Miyasaka, T. Li, J. Ishizuka, T. Arakawa, Y. Shiota, T. Moriyama, Y. Yanase, and T. Ono, Nature (London) **584**, 373 (2020).
- [6] M. Nadeem, M. S. Fuhrer, and X.-L. Wang, Nat. Rev. Phys. **5**, 558-577 (2023).
- [7] J. Hu, C. Wu, and X. Dai, Phys. Rev. Lett. **99**, 067004 (2007).
- [8] T. Yokoyama, M. Eto, and Y. V. Nazarov, Phys. Rev. B **89**, 195407 (2014).
- [9] Y. Zhang, Y. Gu, P. Li, J. Hu, and K. Jiang, Phys. Rev. X **12**, 041013 (2022).
- [10] A. Costa, J. Fabian, and D. Kochan, Phys. Rev. B **108**, 054522 (2023).
- [11] A. F. Andreev, Zh. Eksp. Teor. Fiz. **49**, 655 (1966). J. Exp. Theor. Phys. **22**, 455-458 (1966).
- [12] C. W. J. Beenakker, Phys. Rev. Lett. **67**, 3836 (1991).
- [13] A. Costa, J. Fabian, and D. Kochan, Phys. Rev. B **98**, 134511 (2018).
- [14] M. Davydova, S. Prembabu, and L. Fu, Sci. Adv. **8**, eabo0309 (2022).
- [15] D. B. Szombati, *et al.*, Nat. Phys. **12**, 568-572 (2016).
- [16] W. Mayer, *et al.*, Nat. Commun. **11**, 212 (2020).
- [17] E. Strambini, *et al.*, Nat. Nanotechnol. **15**, 656-660 (2020).
- [18] A. A. Golubov, M. Yu. Kupriyanov, and E. Il'ichev, Rev. Mod. Phys. **76**, 411 (2004).
- [19] C. Baumgartner, *et al.*, J. Phys.: Condens. Matter **34**, 154005 (2022).
- [20] C. Baumgartner, L. Fuchs, A. Costa, S. Reinhardt, S. Gronin, G. C. Gardner, T. Lindemann, M. J. Manfra, P. E. Faria Junior, D. Kochan, J. Fabian, N. Paradiso, and C. Strunk, Nat. Nanotechnol. **17**, 39 (2022).
- [21] A. Costa, *et al.*, Nat. Nanotechnol. 10.1038/s41565-023-01451-x (2023).
- [22] S. Reinhardt, *et al.*, Preprint at arXiv <https://www.arxiv.org/abs/2308.01061v1>.
- [23] A. Varykhalov, J. Sanchez-Barriga, A. M. Shikin, C. Biswas, E. Vescovo, A. Rybkin, D. Marchenko and O. Rader, Phys. Rev. Lett. **101**, 157601 (2008).
- [24] D. Marchenko, A. Varykhalov, M. R. Scholz, G. Bihlmayer, E. I. Rashba, A. Rybkin, A. M. Shikin, and O. Rader Nat. Commun. **3**, 1232 (2012).
- [25] A. Avsar, J. Y. Tan, T. Taychatanapat, J. Balakrishnan, G. K. W. Koon, Y. Yeo, J. Lahiri, A. Carvalho, A. S. Rodin, E. C. T. O'Farrell, G. Eda, A. H. Castro Neto, and B. Ozyilmaz, Nat. Commun. **5**, 4875 (2014).
- [26] M. Gmitra and J. Fabian, Phys. Rev. B **92**, 155403 (2015).
- [27] Z. Wang, D. K. Ki, H. Chen, Berger H, A. H. MacDonald, and A. F. Morpurgo, Nat. Commun. **6**, 8339 (2015).
- [28] P. Wei, S. Lee, F. Lemaitre, L. Pinel, D. Cutaia, W. Cha, F. Katmis, Y. Zhu, D. Heiman, J. Hone, et al., Nature Mater. **15**, 711 (2016).
- [29] Z.-H. Wang, E. V. Castro, and H.-Q. Lin, Phys. Rev. B **97**, 041414(R) (2018).
- [30] C.-C. Tseng *et al.*, Nano Lett. **22**, 8495-8501 (2022).
- [31] C. L. Kane and E. J. Mele, Phys. Rev. Lett. **95**, 146802 (2005).
- [32] Z.-H. Qiao *et al.*, Phys. Rev. B **82**, 161414(R) (2010).
- [33] A. H. Castro Neto, F. Guinea, N. M. R. Peres, K. S. Novoselov, and A. K. Geim, Rev. Mod. Phys. **81**, 109 (2009).
- [34] C. W. J. Beenakker, Rev. Mod. Phys. **80**, 1337 (2008).
- [35] W. Kim, J. Riikonen, C. Li, Y. Chen, and H. Lipsanen, Nanotechnology **24**, 395202 (2013).
- [36] G. Nanda, *et al.*, Nano Lett. **17**, 3396-3401 (2017).
- [37] Gil-Ho Lee and Hu-Jong Lee, Rep. Prog. Phys. **81**, 056502 (2018).
- [38] H. Zhang, J. Wang, and J.-F. Liu, Appl. Phys. Lett. **108**, 102601 (2016).
- [39] Q.-F. Liang, Y. Yu, Q. H. Wang, and J. M. Dong, Phys. Rev. Lett. **101**, 187002 (2008).

- [40] We consider that the system width in the y direction is very large, and the periodic boundary condition is adopted, such that the wave vector k_y is a good quantum number. Thus, by calculating the supercurrents of each k_y -channel and summing them up, one can construct the transport properties of the entire two-dimensional graphene Josephson junction.
- [41] C. Caroli *et al.*, J. Phys. C **4**, 916 (1971).
- [42] M. P. Lopez-Sancho *et al.*, J. Phys. F **14**, 1205 (1984).
- [43] E. I. Rashba, Phys. Rev. B **79**, 161409(R) (2009).
- [44] J. Linder, T. Yokoyama, D. Huertas-Hernando, and A. Sudbø, Phys. Rev. Lett. **100**, 187004 (2008).
- [45] A. M. Black-Schaffer and J. Linder, Phys. Rev. B **82**, 184522 (2010).